Journal of Theoretical Biology 382 (2015) 34–43

Contents lists available at ScienceDirect

Journal of Theoretical Biology

journal homepage: www.elsevier.com/locate/yjtbi

Reconstruction of muscle fascicle architecture from iodine-enhanced microCT images: A combined texture mapping and streamline approach

Kornelius Kupczik [a,b,c,*], Heiko Stark [c,d], Roger Mundry [b], Fabian T. Neininger [e], Thomas Heidlauf [e,f], Oliver Röhrle [e,f]

[a] Max Planck Weizmann Center for Integrative Archaeology and Anthropology, Leipzig, Germany
[b] Max Planck Institute for Evolutionary Anthropology, Leipzig, Germany
[c] Institute of Systematic Zoology and Evolutionary Biology with Phyletic Museum, Friedrich-Schiller-University Jena, Jena, Germany
[d] Department of Bioinformatics, Friedrich-Schiller-University Jena, Jena, Germany
[e] Stuttgart Research Centre for Simulation Technology (SimTech), Universität Stuttgart, Stuttgart, Germany
[f] Institute of Applied Mechanics (CE), Chair of Continuum Mechanics, Universität Stuttgart, Stuttgart, Germany

HIGHLIGHTS

- Knowledge of fascicle architecture is crucial for detailed models to analyse skeletal muscle mechanics.
- Contrast-enhanced μCT-imaging resolves muscle fascicles.
- Pattern recognition and streamlines reconstruct spatial arrangement of fascicles.
- Comparison with fascicle lengths and pennation angles gained from cadaver dissection.

GRAPHICAL ABSTRACT

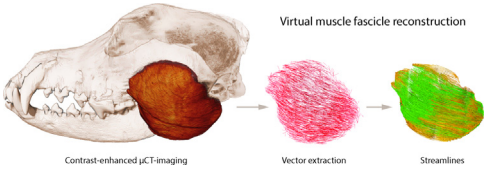

ARTICLE INFO

Article history:
Received 14 August 2014
Received in revised form
8 May 2015
Accepted 20 June 2015
Available online 30 June 2015

Keywords:
Muscle modelling
Masseter muscle
Iodine potassium iodide
Pennation angle
Dog

ABSTRACT

Skeletal muscle models are used to investigate motion and force generation in both biological and bioengineering research. Yet, they often lack a realistic representation of the muscle's internal architecture which is primarily composed of muscle fibre bundles, known as fascicles. Recently, it has been shown that fascicles can be resolved with micro-computed tomography (μCT) following staining of the muscle tissue with iodine potassium iodide (I_2KI). Here, we present the reconstruction of the fascicular spatial arrangement and geometry of the superficial masseter muscle of a dog based on a combination of pattern recognition and streamline computation. A cadaveric head of a dog was incubated in I_2KI and μCT-scanned. Following segmentation of the masseter muscle a statistical pattern recognition algorithm was applied to create a vector field of fascicle directions. Streamlines were then used to transform the vector field into a realistic muscle fascicle representation. The lengths of the reconstructed fascicles and the pennation angles in two planes (frontal and sagittal) were extracted and compared against a tracked fascicle field obtained through cadaver dissection. Both fascicle lengths and angles were found to vary substantially within the muscle confirming the complex and heterogeneous nature of skeletal muscle described by previous studies. While there were significant differences in the pennation angle between the experimentally derived and μCT-reconstructed data, there was congruence

* Corresponding author at: Max Planck Weizmann Center for Integrative Archaeology and Anthropology, Max Planck Institute for Evolutionary Anthropology, Deutscher Platz 6, 04103 Leipzig, Germany. Tel.: +49 341 3550 861.
E-mail address: kornelius_kupczik@eva.mpg.de (K. Kupczik).

http://dx.doi.org/10.1016/j.jtbi.2015.06.034
0022-5193/

in the fascicle lengths. We conclude that the presented approach allows for embedding realistic fascicle information into finite element models of skeletal muscles to better understand the functioning of the musculoskeletal system.

1. Introduction

Muscles, tendons and bones are the fundamental components of the locomotory and masticatory system. While the three-dimensional structure of cortical and cancellous bone tissue has been revealed by histological or imaging techniques, there is much less information available on the complex internal architecture of skeletal muscle. Skeletal muscles are attached via tendons to bones, are the force generating elements, and exhibit a hierarchical structure. Analysing the hierarchical structure, one observes that muscles consist of fascicles, also known as muscle fibre bundles. These typically contain 50 to 400 muscle fibres depending on muscle type, age and species (e.g. Grotmol et al., 2002; Lexell and Downham, 1991). A fibre, in turn, consists of myofibrils, in which sarcomeres (the smallest contractile unit) are sequentially arranged. Force is generated through the interaction of actin and myosin filaments via cross-bridges (Huxley, 1957) and the resulting relative movement of these filaments (Huxley and Niedergerke, 1954). The force transmission occurs through aponeuroses and tendons (Monti et al., 1999).

One of the most common approximations of the muscle force output is the physiological cross sectional area (PCSA), which is based on muscle volume as well as the mean length and pennation angle of the fascicles at selected regions within the muscle (cf. Gans and Bock, 1965; Lee et al., 2012; Lieber and Fridén, 2000; Ravichandiran et al., 2010). Muscle forces derived from PCSA computations are commonly used in multibody dynamic analyses and as boundary conditions in finite element (FE) analyses of the bony masticatory apparatus (Gröning et al., 2013; Grosse et al., 2007; Kupczik et al., 2009; Ross et al., 2005). However, this single value approach is an oversimplification and, in the case of simulations of feeding function, there are apparent discrepancies between PCSA based bite force estimates and experimentally derived force data (Davis et al., 2010). For more realistic muscle models, it is therefore pertinent to take into account the complex geometric arrangement of the fascicles within the entire muscle (Röhrle and Pullan, 2007). Moreover, many physiological principles of skeletal muscle mechanics can only be investigated using a more detailed and realistic representation of the fibre bundles within the muscle model as it is the case with chemo-electro-mechanical (CEM) models as proposed by Röhrle (2010) and Heidlauf and Röhrle (2013, 2014). For their use within volumetric muscle models, fascicle distributions can be approximated, for example, by fitting fascicle templates to muscle outer geometries obtained from MRI data (Blemker and Delp, 2005), or by combining the digitised information of the muscle insertion and origin with techniques known from elliptic grid generation (Choi and Blemker, 2013; Knupp and Steinberg, 1993). Furthermore, based on a detailed data set of digitised fibres from a cadaver, Sánchez et al. (2014) have developed a workflow to embed the digitised fibres within subject-specific muscle geometries.

Muscle internal architecture is commonly investigated by way of histology and anatomical preparations (Ackerman, 1998; Poelstra et al., 2000; Stark and Schilling, 2010; Stark et al., 2013). In addition, various imaging modalities have been employed such as ultrasound (Namburete et al., 2011; Rana and Wakeling, 2011) or diffusion tensor magnetic resonance imaging (DTI; Heemskerk et al., 2005; Infantolino et al., 2012; Lansdown et al., 2007; Schenk et al., 2013; Sieben et al., 2013). Yet, the above techniques have inherent limitations such as the loss of muscle tissue (anatomical preparation) or image noise and limited tissue contrast (ultrasound, DTI). To overcome the above methodological constraints, contrast-enhanced computed tomography (CT) scanning has recently been successfully applied to image with high resolution muscles tissue and other soft tissue parts in various vertebrate species (e.g. fish and amphibians: Metscher, 2009; reptiles: Tsai and Holliday, 2011; birds: Lautenschlager et al., 2014; mammals: Cox and Jeffery, 2011; Jeffery et al., 2011).

Here, we present a novel approach to visualise the fascicle directions in one of the chewing muscles of a dog based on a contrast-enhanced μCT dataset, and use a pattern recognition algorithm to extract individual fascicle representations in 3D. To this end, we computed a vector field, in which each vector direction represents the local orientation of a portion of a fascicle within the muscle. This is based on the assumption that the standard deviation of grey values per voxel in the CT dataset is lower along the fascicle than perpendicular to it. This approach is similar to gradient based methods (Sachse et al., 1998; Varela et al., 2013), but uses a statistically approach. The vector field of fascicle directions is then used to compute streamlines representing individual fascicle distributions. Streamlines are typically used in engineering-like applications to visualise vector fields, e.g., the velocity field of a fluid (e.g. Chong et al., 1990). The present method of computing the respective streamlines uses finite element basis functions to interpolate the discrete vector field of fascicle directions as a continuum field, and thus takes into account directional changes within a voxel. Furthermore, key lumped parameters such as fascicle lengths and pennation angle are extracted from (i) the vector field of fascicle directions, and (ii) the streamline-based fascicle representation. The extracted data are then compared against data derived from muscle dissection.

2. Material and methods

2.1. Specimen preparation and iodine incubation

The head of a domestic dog (medium-sized Bearded Collie mix, female, 11 years old, body mass unknown), obtained *post mortem* from a veterinary clinic and accessioned to the collections of the Phyletisches Museum (Jena, Germany), was dissected and the skin removed. The jaw was closed with the upper and lower teeth in near centric occlusion. Thus, the chewing muscles were assumed to be in their natural, relaxed position. The head was cut in the sagittal plane and one half was fixed in a 4% formalin solution with phosphate buffered saline (PBS) for six weeks. Although formalin fixation may have an effect on (isolated) muscle tissue density and volume (Ward and Lieber, 2005; Vickerton et al., 2013), this was not taken into account as the muscles in question within this study were still in situ attached to the bones. The specimen was subsequently taken out of the solution and rinsed with aqua dest. and PBS for one day. Using a fine grade needle the masticatory muscles were injected with a 25% iodine potassium iodide solution (I_2KI, also known as Lugol's solution) dissolved in PBS. The head was then submerged in the solution and incubated for 14 days to allow for passive diffusion at room temperature. Following this, the head was transferred to a 15% I_2KI solution and incubated for a further week. Although formalin fixation and a high concentration

of I_2KI may lead to a reduction in fascicle lengths and thus changes in the geometry and the pennation angles within the muscle (Cutts, 1988; Cutts and Seedhom, 1993; Ward and Lieber, 2005; Vickerton et al., 2013), this was not taken into account in the present study because we did not aim to compare fresh to fixed muscle tissue architecture.

2.2. Computed tomography and image segmentation

The I_2KI-stained head was scanned in air using a BIR ACTIS 225/300 high-resolution industrial μCT system (Max Planck Institute for Evolutionary Anthropology, Leipzig, Germany) at 130 kV and 0.1 mA with a 0.5 mm brass filter. The resulting tiff images were reconstructed in 8 bit and had an isometric voxel size of 0.064 mm × 0.064 mm × 0.064 mm. The skull and one of the muscles of mastication (superficial masseter) was segmented and visualised in Avizo 7 (Visualization Sciences Group Inc.). The μCT dataset was then cropped to contain the superficial masseter muscle only and exported as a new image stack for further processing. Following μCT scanning, the head was returned to a 4% PBS buffered formalin solution.

2.3. Pattern recognition

The image stack was imported into custom written software 'image3d' (http://starkrats.de). The fascicle directions were analysed by recognizing and distinguishing the image texture, which essentially constitutes a repeated periodically or quasi-periodically pattern (Jähne, 2005). We expected that along a fascicle, which is represented by an array of voxel of a certain distribution of grey values, the standard deviation (SD) of the grey values would be lowest. In contrast, when moving away from this array, or being perpendicular to it, there would be an increase in SD of grey values. By taking into account all possible fascicle directions, we thus generated an orientation map that describes the orientation of the texture in a defined region.

The following operational steps were performed: (i) Enhancement of the image characteristics to obtain a better contrast-to-noise ratio. This was done by adjusting the intensity range to span the entire 8 bit range and by highlighting the edges by unsharp masking (gauss filter=1). (ii) Generation of an orientation map (planar image projection of a hemisphere) for a single μCT voxel. To this end, for a hemisphere pixel the standard deviation (SD) from all grey values along the maximum straight distance through the sphere was computed (Alemán-Flores and Álvarez-León, 2003). This was done for each hemisphere pixel and resulted in 1609 tracks for a given sphere radius of 16 voxel ($A_{\text{hemisphere}} = 2{*}\pi{*}(16)^2$). Of these SD, the global minimum was determined, the resulting vector was stored, and the remaining SD computations were discarded. This operation was repeated for each voxel resulting in a complex vector field, in which the normalised vector length is multiplied by the minimal SD (cf. Fig. S1). (iii) Finally, local vectors were binned (9 × 9 × 9 voxel) to reduce noise and to simplify the vector field.

2.4. Muscle fascicle tracking by means of streamlines

The vector field of fascicle directions was first normalised to unit length. This contribution appeals to the calculation of streamlines to transform the vector field into a realistic muscle fascicle representation. Furthermore, finite element basis functions were used to interpolate the surrounding fascicle orientations at each point along a tracked fascicle, i.e., the distances between the current tracking point and the points of the vector field are used as weights for the interpolation. Computing streamlines in conjunction with finite element interpolation, directional changes of the tracked fascicles within a voxel are possible. This provides the basis for an accurate and smooth representation, even for low-resolution vector fields.

In fluid dynamics, streamlines are snapshots of the local tangent directions to the velocity field at an instant in time. In general, streamlines are the solution to the differential equation

$$dx(\sigma)/d\sigma = v(x(\sigma), t) \tag{1}$$

with initial condition

$$x(\sigma_0) = x_0,$$

where x denotes a position in space, σ is the parameter of the streamline, t is the time, v denotes the velocity field, and x_0 is a seed point of the streamline. To determine muscle fascicle directions, it is sufficient to consider steady-state conditions, where streamlines and pathlines coincide and the velocity field does not explicitly depend on time, i.e., it reduces to $v(x(\sigma))$. In the context of fascicle tracking, the velocity field v is replaced by the vector field of fascicle directions. The first-order accurate forward (explicit) Euler method is used to discretise Eq. (1):

$$x_{k+1} = x_k + \Delta\sigma\, v(x_k)$$

wherein $\Delta\sigma = \sigma_{k+1} - \sigma_k$ denotes the step size, $x_k = x(\sigma_k)$, and $\sigma_k = \sigma_0 + k\Delta\sigma \quad (k = 0, 1, 2, \ldots)$. In this contribution, finite elements are used to approximate the vector field at position x_k, i.e.,

$$x_{k+1} = x_k + \Delta\sigma \sum_e \sum_n \varphi_n(x_k) v_n,$$

wherein φ_n is a finite element basis function, and v_n denotes the fascicle direction of the vector field at node n of the corresponding finite element e. Here, tri-linear Lagrange finite elements of size 9 × 9 × 9 voxel were applied (see Section 2.3). The step size for the streamline calculation was chosen to be equivalent to 0.5 voxel, i.e., to 0.032 mm.

To find seed points for the streamline calculation, three parallel, rectangular planes were defined that intersect the muscle at different locations approximately perpendicular to the fascicle direction. Seed points were defined at equidistant locations on the planes. Starting from each seed point the streamline calculation was initiated in both directions of the plane. Seed points for which no surrounding finite element could be determined, i.e., points lying outside of the muscle geometry, were discarded. A single plane of seed points was not sufficient to generate streamlines with an adequate density in the entire muscle geometry, hence, the choice of three planes (cf. Heemskerk et al., 2005). The algorithm stopped, when a streamline left the muscle geometry, i.e., no surrounding finite element was be identified that determined the streamline's direction.

The positions of the finite element nodes are determined by the locations at which the pattern recognition algorithm computed the fascicle directions. These points were chosen in this work as evenly distributed. The easiest and the most straightforward approach of generating a finite element mesh out of evenly distributed points is to connect neighbouring points in order to form regular hexahedral (brick-shaped) elements. The resulting mesh essentially resembles a voxel-based mesh. For objects with complex surfaces, voxel-based meshes can only approximate the object and are never exact. The approximation improves as the size of the hexahedral elements reduces; within this work, however, the size of these elements is determined by the pattern recognition algorithm. As a result of the voxel-based mesh, there exist seed points for the streamlines so close to the surface that no further streamline direction can be determined anymore already after a few integration steps. This leads to non-physiological short streamlines that need to be discarded. Streamlines less than 10% of the mean streamline-based fascicle length were considered in this work as non-physiological. Hence, all streamlines consisting of less

than 100 points, i.e. streamlines that are shorter than 3.2 mm, were discarded. Note that a finer voxel-based mesh would reduce the number of short streamlines. Likewise, fascicles longer than those found in the dissection were regarded as non-physiological and hence excluded (i.e., >40.78 mm or 1275 points, respectively).

The perl (http://www.perl.org/) scripts and MATLAB (The MathWorks, Inc., Natick, MA, USA) functions used for preprocessing, streamline generation and export are provided in the Supplementary material.

2.5. Extraction of muscle anatomical data from model

Fascicle lengths in the masseter muscle were estimated based on 2202 generated streamlines (three planes of equally spaced seed points with 9 voxel distance between adjacent seed points). Based on the number of points in a streamline and the distance between two consecutive points (0.032 mm; see above), the total length of the streamline was determined. The streamlines and the vector field were visualised using cmgui (http://www.cmiss.org/cmgui).

Pennation angles were determined from both the vector field and the streamlines. Angles were computed in two planes (frontal and sagittal) by using custom-made software 'Cloud2' (http://starkrats.de) (Fig. S2). The angle for each vector was calculated and then averaged for all vectors along the force direction.

2.6. Dissection-based retrieval of muscle anatomical data

To obtain real anatomical data for comparison, the dog head was fixed with the flat side onto a dissection board and a reference frame with four marker points was defined on the board in order to take into account any possible movements during subsequent data capture (Fig. S3). The connective tissue covering the masseter muscle was then removed with scalpel dissection to expose the lateral aponeurosis. Each identifiable fascicle on the exposed muscle surface was tracked along its entire distance with a 3D-Microscribe G2 (Immersion Corporation, San Jose, CA). While the producer specified accuracy is 0.38 mm, we established a mean intra-observer error of 1.01 ± 0.45 mm based on 136 repeated measurements of four reference points. Subsequently, the first fascicle layer was removed and the newly exposed fascicle layer was tracked (Fig. S3). The fascicles were distinguished by their fleshy and tendinous portions. This procedure was repeated until all muscle fascicles of the superficial masseter were removed. All fascicle data were processed in Cloud2 to remove movement artefacts and erroneous measurements. In addition, fascicle lengths and pennation angles (see above) were computed in Cloud2.

2.7. Statistical analysis

The means and standard deviations as well as the medians and upper and lower quartiles of both fascicle length and pennation angle were computed for all three datasets (vector field, streamlines, and dissection). The Shapiro–Wilk statistic was used to test for normally distributed data. The non-parametric Mann–Whitney *U*-test was employed to assess the independence between the fascicle lengths obtained by the streamline technique and the dissection. The tests were performed in PAST 3.01 (Hammer et al., 2001). Please note that the Mann–Whitney-*U*-test likely suffers from autocorrelation in these measures. However, we believe that a correction for non-independence in the context of this non-parametric test is not straightforward.

To test whether the three different techniques measuring the angles (vector field, streamlines and dissection) systematically deviated from each other, we used permutation tests (Adams and Anthony, 1996; Manly, 2006) conducting pairwise comparisons between the techniques (vector field vs. dissection; streamlines vs. dissection; streamlines vs. vector field). In a first step, we measured the angular distance between each angle (in radians) and the mean angle of the respective method as well as the angular difference between the mean angles of each of the two methods compared. To compute the test statistic quantifying the magnitude of difference between two techniques (the relative angular distance between the two group means) we proceeded as follows: (i) we determined the mean angle per technique and then the average angle between each particular angle and the mean of the respective technique ('mean angle within'). (ii) We determined the angle between the two mean angles per technique ('angle between'). (iii) The test statistic was derived by dividing 'angle between' by the sum of the two values of mean angle within. We subsequently randomized the data 1000 times (including the original data as one permutation). Since the data were of a related design (i.e. each technique was applied to angles at the same position along the principal direction of force) we randomized angles between methods but keeping their position along this axis. We determined the test statistic for each of the randomizations and determined the final *p*-value as the proportion of permutations revealing a test statistic at least as large as the original angle. This approach was applied to each pair of techniques. We are aware that this method does not appropriately account for the presumably strong autocorrelation in the measured angles but an easy fix to this problem is not known to us. All analyses were programmed and conducted in R (version 3.1.0, R Core Team, 2014).

3. Results

3.1. Muscle staining and reconstruction

The μCT scanning of the head revealed that in particular the outer soft tissue regions were successfully stained by the I_2KI solution. Thus, this allowed for the visualisation of the anatomy and internal fascicle architecture of the superficial masseter (Figs. 1 and 2). Near the muscle surface, the fascicles and their orientation are clearly visible through volume renderings of the μCT dataset (Fig. 3). The fascicles describe a curvilinear path when viewed laterally starting at the muscle's origin under the zygomatic arch and ending at the insertion area at the lower border of the mandibular ramus (Figs. 2 and 3). The total length of the superficial masseter from origin to insertion along the long axis of the muscle was measured to be 55.7 mm using Avizo 3D rendering. The fascicle arrangement is represented by a total of 3683 vectors and 2202 streamlines, respectively (Fig. 4). In the dissection, we recorded 1719 data points equalling 203 fascicles (on average nine points per fascicle) of which 30 fascicles were part of the lateral aponeurosis.

3.2. Fascicle lengths

The streamline calculation predicted a maximum fascicle length of 56.7 mm which is close to the total muscle length reported above (Fig. 5). This stands in contrast to the longest fascicle tracked in the dissection, i.e. 40.78 mm. Based on the Shapiro–Wilk test, neither the experimentally derived fascicle lengths nor the streamline-based results were normally distributed ($W_{exp}=0.9523$; $p<0.0001$; $W_{stream}=0.9513$; $p<0.0001$; Fig. 5). The Mann–Whitney *U*-test revealed a significant difference between the medians of the two fascicle length distributions ($n_{diss}=173$, $n_{str}=2202$, $U=1.0588\times10^5$, $p<0.0001$; Table 1). Since a large number of the generated streamlines ($n=799$; about 1/3 of

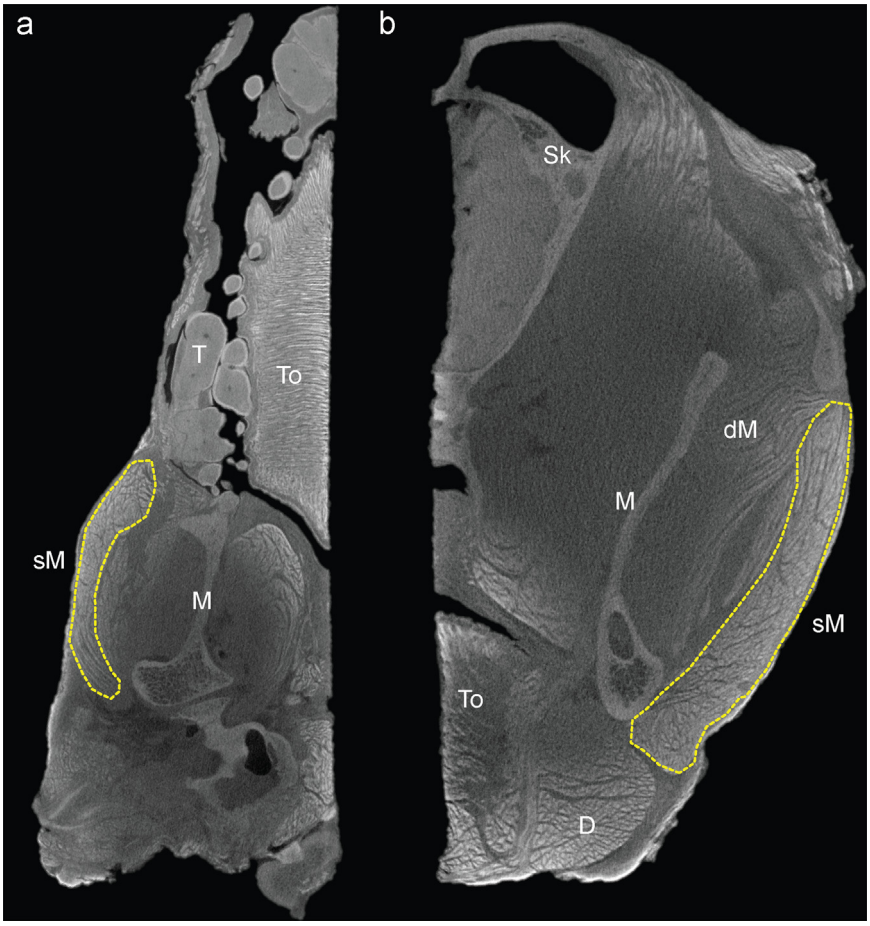

Fig. 1. μCT images of I_2KI stained head showing soft tissue regions. (a) Transverse section through the upper third of the superficial masseter (sM; outlined in yellow). (b) Coronal section halfway through superficial masseter. Note that outer regions show better contrast than towards the centre of the head. Abbreviations: D=digastricus muscle, M=mandible, dM=deep masseter muscle, Sk=skull, T=tooth, To=tongue. (For interpretation of the references to color in this figure legend, the reader is referred to the web version of this article.)

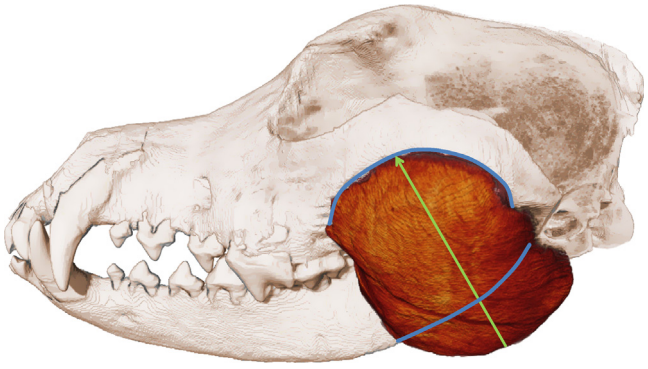

Fig. 2. Volume rendering of dog skull in lateral view with left superficial masseter muscle shown in red. Blue solid line indicates the origin of the muscle below the zygomatic arch and blue stippled line indicates insertion of muscle at the base of the mandibular ramus (not visible). Green solid line shows line of action during muscle contraction.

the total dataset) were longer than the longest experimentally determined fascicle (see Fig. 5), any fascicle longer than 40.78 mm was removed from the streamline dataset and the statistics were re-run (reduced streamlines; Table 1). In this case, the Mann–Whitney *U*-test predicted no significant difference between the median lengths of the experimentally determined fascicles and the reduced streamline dataset ($n_{diss}=173$, $n_{stred}=1403$, $U=1.1479\times10^5$, $p=0.245$). The fascicles with a length of up to 40.78 mm were distributed throughout the muscle, while the fascicles longer than this value were concentrated on the lateral surface of the upper half of the muscle (Fig. 4). The latter were part of the aponeurosis overlaying the masseter muscle and ran through the centre of the muscle (Fig. 4; aponeurosis not visible). With regard to volumetric proportions, the dataset was comprised of 49% fascicles with up to 40.78 mm and 51% of fascicles with more than 40.78 mm.

3.3. Pennation angles

The angular distances between the dissection technique and those derived from the vector field and the streamlines (full dataset) were considerably larger than those between the vector field and streamlines (Table 2; Fig. 6). The pennation angles of the reduced streamline dataset (representing the physiological fascicles shorter than 40.78 mm; see above) compare somewhat better with the dissection derived values (Table 2; Fig. 6). All three tests comparing two techniques at a time revealed clear significance (permutation test: all $p=0.001$; Table 3). The difference between the angular measurements was particularly large at the origin and insertion of the muscle (Fig. 6).

4. Discussion

Contrast-enhanced CT scanning has already been widely employed to investigate muscle gross anatomy in a number of

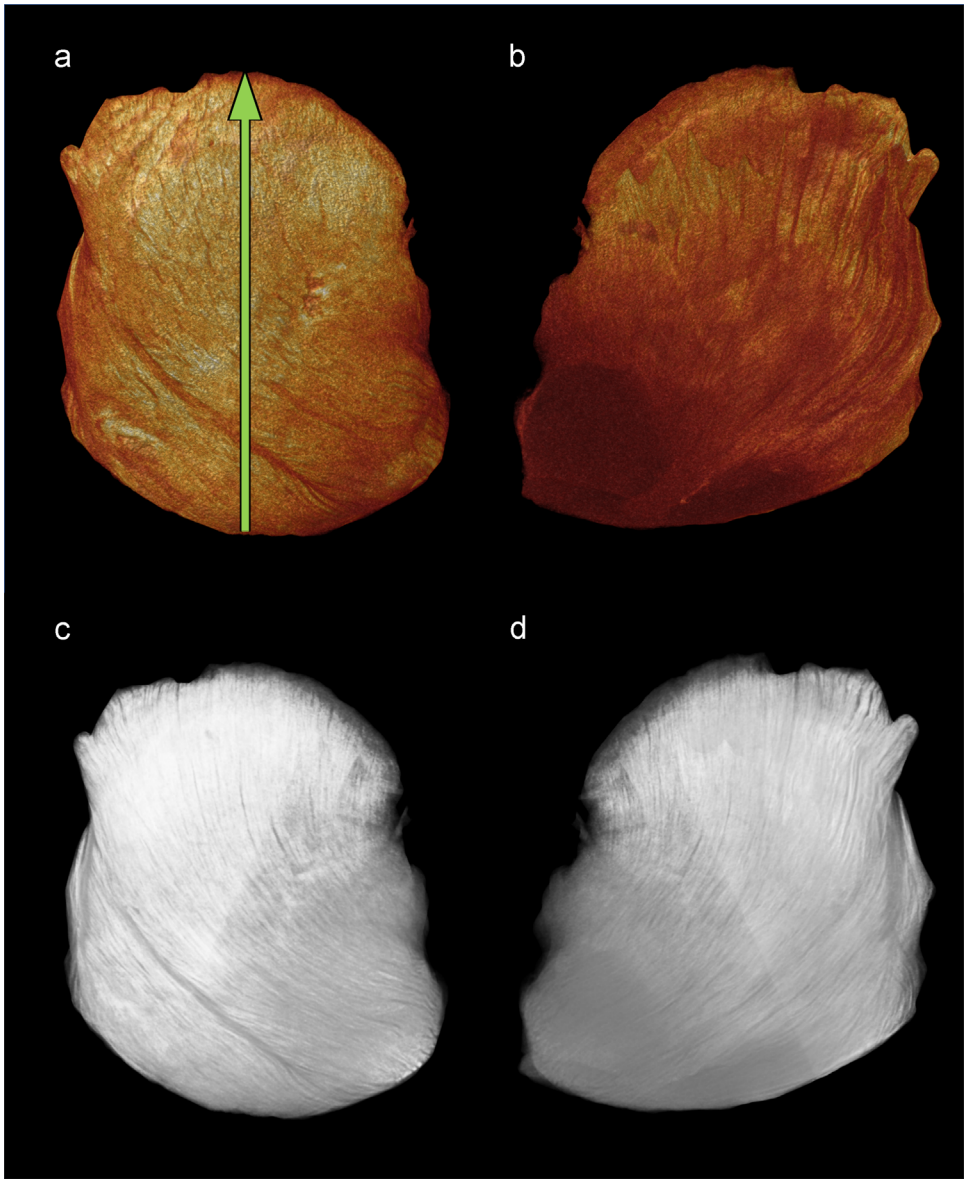

Fig. 3. Left superficial masseter muscle in lateral (a and c) and medial views (b and d) to show outer and inner fascicle architecture ((a) and (b) volume renderings; (c) and (d) maximum intensity projections with 75% transparency). Note that the muscle is rotated in the sagittal plane such that the muscle force vector (shown in green) is aligned vertically.

vertebrate species varying in body size (e.g. Cox and Jeffery, 2011; Holliday et al., 2013; Lautenschlager et al., 2014; Tsai and Holliday, 2011; Vickerton et al., 2013). In addition, Kupczik et al. (2007) reconstructed the volume of a superficial masseter of a macaque from the unstained medical CT scans of a dehydrated specimen to build a finite element model. However, the low resolution of the CT scans did not allow for the reconstruction of the internal fascicle architecture. Yet, Jeffery et al. (2011) convincingly demonstrated the potential of iodine-enhanced CT scanning in resolving muscle fascicles. The present study takes this a step further by using a combined approach to visualise, quantify, and analyse the external and internal architecture of the superficial masseter muscle of a dog. Both fascicle lengths and pennation angle were found to vary substantially depending on the location within the muscle. This concurs with previous studies showing the complex and heterogeneous architecture of skeletal muscle (Gorb and Fischer, 2000; Infantolino et al., 2012; Schenk et al., 2013; Stark and Schilling, 2010). Thus, the use of single values for fascicle length and pennation angle in PCSA computations or Hill-type muscle models results in significant underestimations in force output and has to be treated with caution (cf. Stark and Schilling, 2010).

The advantage of generating such detailed data and geometrical models is two-fold. First, by considering the geometrical data such as the fascicle distribution and its spatial arrangement, one can gain completely new insights into muscle anatomy. For example, the observed curvilinear path of the fascicles from the zygomatic arch to the angle of the mandible (see Fig. 3) differs from what has previously been reported on the dog's superficial masseter anatomy (Strom et al., 1988). The spatial arrangement is also markedly distinct from that found in the human superficial masseter (i.e., parallel fascicle arrangement approximately 45 degrees relative to zygomatic arch; (cf. Schumacher, 1961). Second, by combining detailed geometrical data of a muscle with biophysically based models based on muscle contractile and deformation properties (e.g. Siebert et al., 2008; Böl et al., 2013), one obtains completely new insights and approaches to analyse the kinematics and dynamics of the musculoskeletal system. This is particularly

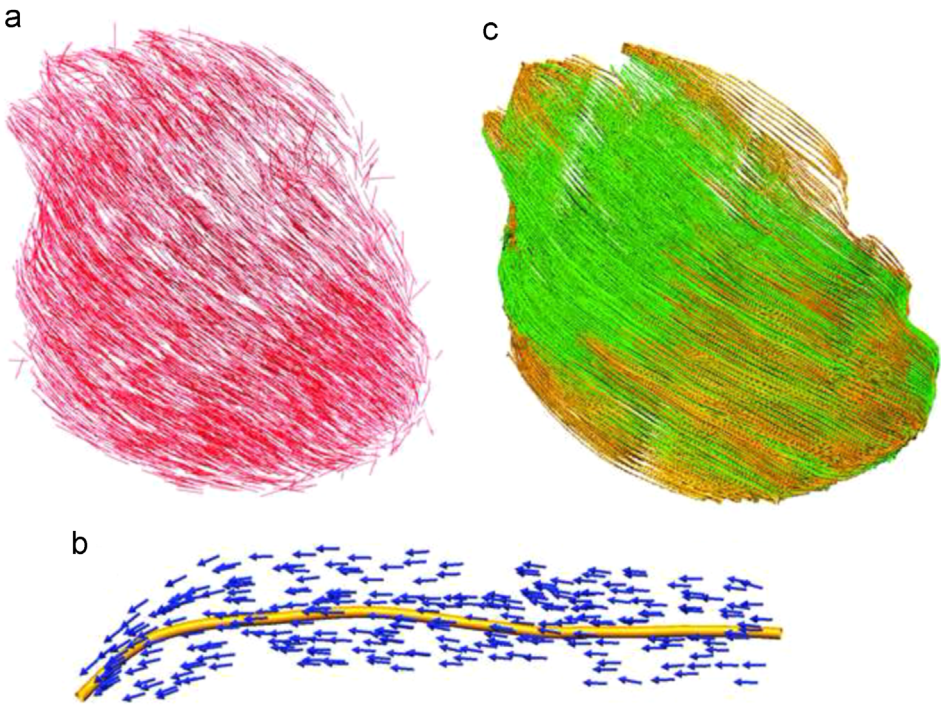

Fig. 4. (a) Lateral view of the calculated vector field. Only ~1% of the normalised vectors are shown. (b) Single long (44.1 mm length) streamline with adjacent vectors computed from vector field. The selected streamline is located in the interior of the muscle. (c) Lateral view of 2202 calculated streamlines with fascicles up to 40.78 mm in length (gold) and fascicles up to 56.7 mm (green). See text for further details. Note that (a) and (c) use the same orientation as is used in Fig. 3.

true if one appeals to CEM models as proposed by Heidlauf and Röhrle (2013, 2014) and Mordhorst et al. (2015).

4.1. Comparison between anatomically derived and μCT-reconstructed data: methodological caveats

The two principal variables characterising the internal architecture of a muscle, namely the lengths and orientations of the fascicles, were extracted. To this end, we determined fascicle lengths and pennation angles by way of dissection, and compared these values with those generated from the μCT reconstruction. If only a subset of the reconstructed fascicles (streamlines reduced) was considered, the fascicle lengths were comparable to those tracked as part of the dissection (Table 1; Fig. 5). At the same time, however, both techniques (vector field and streamlines) yielded pennation angles streamlines were significantly different from those obtained by muscle dissection (Tables 2 and 3; Fig. 6). These findings concur with those by Schenk et al. (2013), who used DTI to reconstruct the fascicles in a soleus muscle of a rabbit.

In general, both approaches applied here – the fascicle digitization and the μCT reconstruction – have their own inherent limitations. The error of the dissection-based method is due to the limited accuracy of the manual operation of the 3D digitizer and of the device itself (cf. Sánchez et al., 2014). Moreover, the fascicle digitization yielded less than half the data points (1719) than what was possible with the μCT reconstruction (3683) (cf. Schenk et al., 2013).

The μCT reconstruction yielded streamlines that were either significantly shorter or longer than the fascicles obtained by manual digitization. It is noteworthy that the unnaturally long (i.e. longer than 40.78 mm) fascicles spanned nearly over the entire length of the muscle, i.e. they originated from the prominent aponeurosis of the dog's superficial masseter (cf. Schumacher, 1961; our Fig. 4). Our muscle dissection revealed that most fascicles ended posteriorly in another aponeurosis, which in turn attaches to the bone surface. Non-physiologically long streamlines can be considered as computational artefacts and should be excluded from the computed data set by optimizing the streamline algorithm. The same applies to very short fascicles (smaller than 3.2 mm; see Section 2.4). To exclude very short fascicles, a better approximation of the muscle geometry is required, e.g. by using a finite element mesh that consists of (hexahedral and) tetrahedral elements. To exclude long fascicles, the anatomical position of the aponeuroses has to be known a priori. If the latter is not known, it is conceivable to introduce a cut-off criterion in an extended version of the algorithm. Moreover, it was recently observed that a high concentration of I_2KI can lead to marked tissue shrinkage during a relatively short incubation period (Vickerton et al., 2013). It is therefore also conceivable that our iodine stained muscle may have decreased in length between the μCT scanning and the dissection at a later date.

With regard to the significant differences in pennation angles between the three methods, a possible reason may be that we did not use a single coordinate system to co-register all datasets (μCT reconstruction and digitization) but only relied on external bone anatomical landmarks for the 3D reconstruction. A co-registration using more readily identifiable markers such as metal screws is recommended for future studies. A further possible source of error is the binning of local vectors to simplify the vector field. The observed statistical difference in the angles between the vector field and the streamline dataset, albeit small in absolute terms, is somewhat surprising. This difference was particularly large at the origin and insertion of the muscle but not in the muscle belly. In the centre of the muscle the vectors were homogenous and thus the algorithm was able to correctly detect the streamlines without the need to use a cut-off criterion. Considering that the muscle output force is related to the physiological cross-sectional area, which in turn depends on the cosine of the pennation angle, the effect of varying angles derived by our reconstruction technique can thus be assessed. Thus, a 5° difference (e.g. compare the medians of 18° and 13° of the dissection and the streamlines, respectively; see Table 2) would result in a difference of about 2%

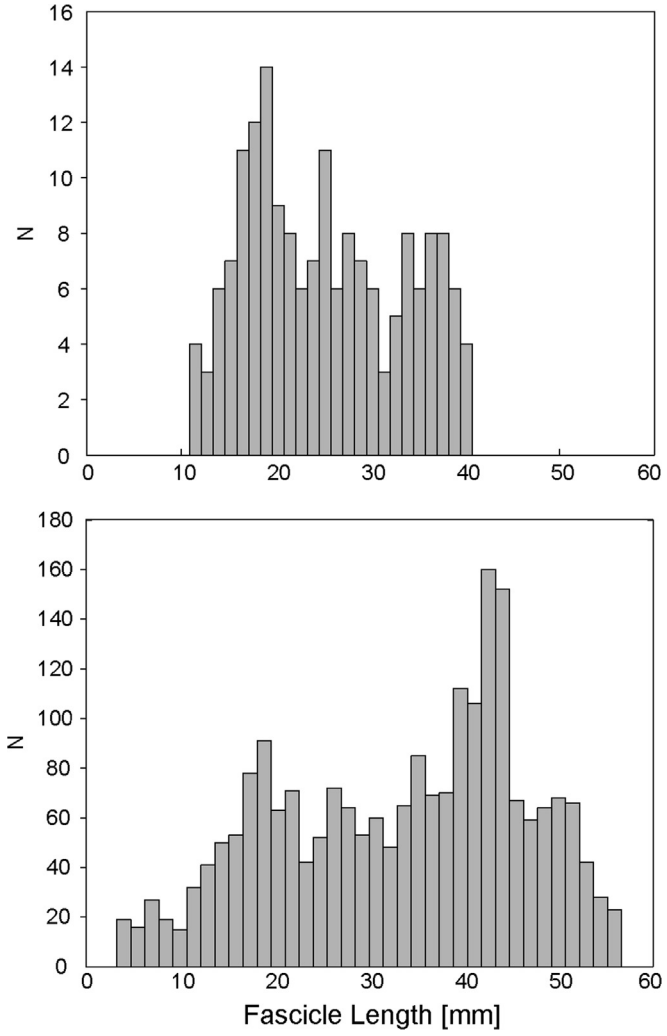

Fig. 5. Histograms of fascicle lengths derived from dissection (top) and streamlines (bottom).

Table 1
Fascicle length statistics in [mm] derived from dissection and streamline computation.

	N	Mean	Std	Q_{25}	Median	Q_{75}
Dissection	173	25.20	8.10	18.39	24.59	32.43
Streamlines	2202	33.30	12.95	22.08	35.68	43.42
Streamlines reduced[a]	1403	25.76	9.88	18.15	26.30	34.82

[a] Streamlines reduced are all streamlines shorter than the longest fascicle measured during dissection with a length of 40.78 mm.

Table 2
Pennation angle statistics in [°].

	Plane	*N*	Mean	Std	Q25	Median	Q_{75}
Dissection	Sagittal	509	11.30	6.69	7.62	4.74	10.85
	Frontal		22.67	8.26	16.69	14.96	27.74
Vectors	Sagittal	509	8.66	3.23	5.67	4.49	10.50
	Frontal		14.50	5.82	10.29	7.39	17.10
Streamlines	Sagittal	509	7.42	3.03	4.55	3.98	9.16
	Frontal		14.85	6.39	9.79	8.23	17.76
Streamlines red	Sagittal	509	7.49	2.46	5.87	7.40	8.38
	Frontal		15.07	3.70	11.97	14.22	19.18

in force output. In contrast, the more heterogeneous distribution of the vectors and the highly concentrated streamlines towards

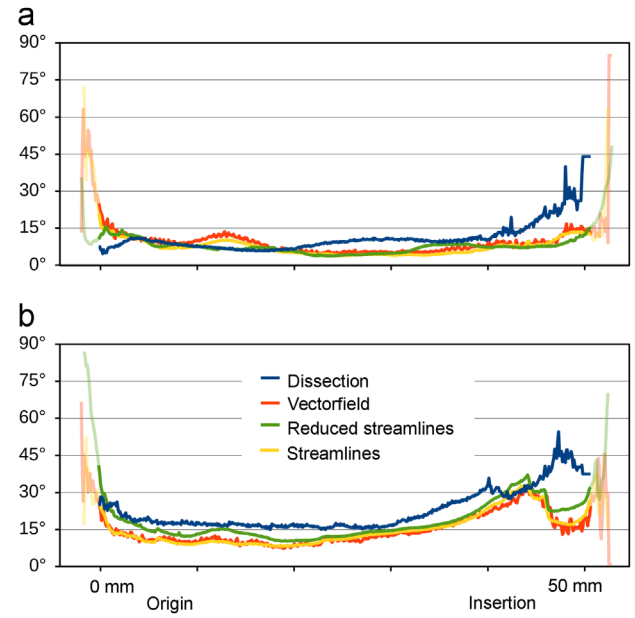

Fig. 6. Pennation angles along the muscle force direction (from origin to insertion) calculated from the anatomical data, vector field, and streamlines (both long and reduced). (a) Pennation angles against the sagittal plane and (b) pennation angles against the frontal plane.

Table 3
Measures of angular distances between angles and their respective group means (mean a within 1 and mean a within 2), between group means (mean a between) and the quotient between the latter and the sum of the two former (test statistic).

	Mean a within 1	Mean a within 2	Mean a between	Test statistic
Dissection vs. vectors	0.142	0.102	0.148	0.607***
Dissection vs. streamlines	0.142	0.108	0.151	0.603***
Dissection vs. streamlines red	0.142	0.071	0.147	0.689***
Vectors vs. streamlines	0.102	0.108	0.022	0.107***
Vectors vs. streamlines red	0.102	0.071	0.023	0.130***

*** $p=0.001$.

the origin and insertion areas in the muscle, yield a larger error in computing the pennation angles (cf. Fig. 4).

The technical limitations notwithstanding, the obtained results allow for some comparison with literature data on the dog's nearest living relative, the grey wolf. The average fascicle lengths of the superficial masseter in an adult male wolf (average body weight of about 33 kg; Gittleman, 1985: 542) is reported to be 32.5 mm and 29.6 mm for the right and left side, respectively (Schumacher, 1961: 140). These values were derived from anatomical preparation, and are close to the present finding (adult female Bearded Collie mix of medium size) of 25.2 mm for the dissection and 25.76 mm for the streamlines (reduced data set), respectively. While this study was limited to the superficial masseter, contrast-enhanced μCT imaging can also be applied to extract anatomical information of more deeply located muscles (see e.g. Jeffery et al., 2011; Cox and Jeffery, 2011; Lautenschlager et al., 2014). This may require an adaptation of the tissue staining protocol (e.g. staining agent, incubation time, concentration, temperature, pressure) to allow for penetration of the entire structure by way of I_2KI or other chemical agents (see Metscher, 2009). Further experiments to improve our approach are currently under way.

4.2. Conclusions

With the above methodological caveats in mind, the presented approach to reconstruct and analyse the internal muscle anatomy has great potential to open up new pathways in gaining a better understanding of the structure and function of the musculoskeletal system. This is particularly true, since the presented pattern recognition methodology providing the data for the streamline calculations is not restricted to the use of contrast-enhanced μCT imaging. The same approach is thus applicable to extract fascicle directions when histology, ultrasound or MRI imaging is employed.

The most significant impact of combining imaging, pattern recognition, and streamline calculations is the 3D reconstruction of muscle-specific fascicle architectures in a relatively simple and straight-forward way. This methodology has the potential for a number of advancements, across both research and education. Indeed, from a visualisation standpoint, it would be possible to significantly improve medical training through the integration of these reconstructions into lectures or e-learning platforms as an interactive 3D visualisation tool. Anatomically-derived reconstructions of muscle architecture are also required for continuum-mechanical models which rely on accurate volumetric representations of muscle fascicle orientation. Accordingly, 3D reconstructions of this nature can provide a new level of sophistication for computational models; particularly if realistic motor unit fibre distributions are also available. This is particularly true for chemo-electromechanical modelling approaches, in which the chemo-electromechanical behaviour of single muscle fibres is simulated and linked to the overall mechanical behaviour in a homogenised way (see Heidlauf and Röhrle, 2014). To this end, the combination of realistic biophysical and mechanical muscle models and anatomically realistic reconstructions of a muscle's architecture provide the foundation for in silico experiments to further improve our understanding of the underlying physiological or pathophysiological mechanisms of muscle contractions and force generation.

Acknowledgements

We are grateful to Nathan Jeffery for advice on I_2KI staining, Matthias Krüger, Katja Felbel and Katja Wachs for lab assistance, Patrick Schönfeld for μCT scanning of the specimen and Benjamin Wipfler for help with image segmentation. We would also like to thank two anonymous reviewers for their comments to improve this manuscript, and to Edwin Dickinson for language editing. Financial support by the Max Planck Society (to KK), the Gesellschaft zur Förderung Kynologischer Forschung e.V. (to KK), the German Ministry for Education and Research (to HS) and the German Social Accident Insurance (DGUV) (Grant no. FF-FR0194, to HS) is gratefully acknowledged. Furthermore, the research leading to these results has received funding from the European Research Council under the European Union's Seventh Framework Programme (FP/2007-2013)/ERC Grant Agreement no. 306757 (LEAD; to OR and TH). Responsibility for the content of this publication lies with the authors.

Appendix A. Supporting information

Supplementary data associated with this article can be found in the online version at http://dx.doi.org/10.1016/j.jtbi.2015.06.034.

References

Ackerman, M., 1998. The visible human project. Proc. IEEE 86, 504–511. http://dx.doi.org/10.1109/5.662875.
Adams, D.C., Anthony, C.D., 1996. Using randomization techniques to analyse behavioural data. Anim. Behav. 51, 733–738.
Alemán-Flores, M., Álvarez-León, L., 2003. Texture Classification Through Multiscale Orientation Histogram Analysis. Scale Space LNCS 2695 , 479-493, http://dx.doi.org/10.1007/3-540-44935-3_33.
Blemker, S.S., Delp, S.L., 2005. Three-dimensional representation of complex muscle architectures and geometries. Ann. Biomed. Eng. 33, 661–673. http://dx.doi.org/10.1007/s10439-005-1433-7.
Böl, M., Leichsenring, K., Weichert, C., Sturmat, M., Schenk, P., Blickhan, R., Siebert, T., 2013. Three-dimensional surface geometries of the rabbit soleus muscle during contraction: input for biomechanical modelling and its validation. Biomech. Model. Mechanobiol. 12, 1205–1220.
Choi, H.F., Blemker, S.S., 2013. Skeletal muscle fascicle arrangements can be reconstructed using a Laplacian vector field simulation. PLoS One 8, e77576. http://dx.doi.org/10.1371/journal.pone.0077576.
Chong, M.S., Perry, A.E., Cantwell, B.J., 1990. A general classification of three-dimensional flow fields. Phys. Fluids A: Fluid Dyn. 2, 765–777. http://dx.doi.org/10.1063/1.857730 1989-1993.
Cox, P.G., Jeffery, N., 2011. Reviewing the morphology of the jaw-closing musculature in squirrels, rats, and guinea pigs with contrast-enhanced microCt (vol 294, pg 915, 2011). Anat. Rec.—Adv. Integr. Anat. Evol. Biol. 294, http://dx.doi.org/10.1002/Ar.21483 1612-1612.
Cutts, A., 1988. Shrinkage of muscle fibres during the fixation of cadaveric tissue. J. Anat. 160, 75.
Cutts, A., Seedhom, B.B., 1993. Validity of cadaveric data for muscle physiological cross-sectional area ratios: a comparative study of cadaveric and in-vivo data in human thigh muscles. Clin. Biomech. 8, 156–162.
Davis, J.L., Santana, S.E., Dumont, E.R., Grosse, I.R., 2010. Predicting bite force in mammals: two-dimensional versus three-dimensional lever models. J. Exp. Biol. 213, 1844–1851.
Gans, C., Bock, W.J., 1965. The functional significance of muscle architecture—a theoretical analysis. Ergeb. Anat. Entwicklungsgesch. 38, 115–142.
Gittleman, J.L., 1985. Carnivore body size: ecological and taxonomic correlates. Oecologia 67, 540–554.
Gorb, S.N., Fischer, M.S., 2000. Three-dimensional analysis of the arrangement and length distribution of fascicles in the triceps muscle of *Galea musteloides* (Rodentia, Cavimorpha). Zoomorphology 120, 91–97. http://dx.doi.org/10.1007/s004350000026.
Gröning, F., Jones, M.E.H., Curtis, N., Herrel, A., O'Higgins, P., Evans, S.E., Fagan, M.J., 2013. The importance of accurate muscle modelling for biomechanical analyses: a case study with a lizard skull. J. R. Soc. Interface 10, 20130216.
Grosse, I.R., Dumont, E.R., Coletta, C., Tolleson, A., 2007. Techniques for modeling muscle-induced forces in finite element models of skeletal structures. Anat. Rec. 290, 1069–1088.
Grotmol, S., Totland, G.K., Kryvi, H., Breistøl, A., Essén-Gustavsson, B., Lindholm, A., 2002. Spatial distribution of fiber types within skeletal muscle fascicles from Standardbred horses. Anat. Rec. 268, 131–136.
Hammer, Ø., Harper, D.A.T., Ryan, P.D., 2001. PAST: paleontological statistics software package for education and data analysis. Palaeontolia Electron., 4.
Heemskerk, A.M., Strijkers, G.J., Vilanova, A., Drost, M.R., Nicolay, K., 2005. Determination of mouse skeletal muscle architecture using three-dimensional diffusion tensor imaging. official journal of the Society of Magnetic Resonance in Medicine/Society of Magnetic Resonance in Medicine. Magn. Reson. Med. 53, 1333–1340. http://dx.doi.org/10.1002/mrm.20476.
Heidlauf, T., Röhrle, O., 2013. Modeling the chemoelectromechanical behavior of skeletal muscle using the parallel open-source software library openCMISS. Comput. Math. Methods Med., 2013. http://dx.doi.org/10.1155/2013/517287.
Heidlauf, T., Röhrle, R., 2014. A multiscale chemo-electro-mechanical skeletal muscle model to analyze muscle contraction and force generation for different muscle fiber arrangements. Front. Physiol. 5, 1–14.
Holliday, C.M., Tsai, H.P., Skiljan, R.J., George, I.D., Pathan, S., 2013. A 3D interactive model and atlas of the jaw musculature of alligator mississippiensis. PLoS One 8, http://dx.doi.org/10.1371/journal.pone.0062806.
Huxley, A.F., 1957. Muscle structure and theories of contraction. Prog. Biophys. Biophys. Chem. 7, 255–318.
Huxley, A.F., Niedergerke, R., 1954. Structural changes in muscle during contraction: interference microscopy of living muscle fibres. Nature 173, 971–973.
Infantolino, B.W., Neuberger, T., Challis, J.H., 2012. The arrangement of fascicles in whole muscle. (Hoboken, N.J.: 2007). Anat. Rec. 295, 1174–1180. http://dx.doi.org/10.1002/ar.22484.
Jähne, B., 2005. Digital Image Processing. Springer.
Jeffery, N.S., Stephenson, R.S., Gallagher, J.A., Jarvis, J.C., Cox, P.G., 2011. Micro-computed tomography with iodine staining resolves the arrangement of muscle fibres. J. Biomech. 44, 189–192. http://dx.doi.org/10.1016/j.jbiomech.2010.08.027.
Knupp, P.M., Steinberg, S., 1993. Fundamentals of Grid Generation. CRC Press, Boca Raton, FL.
Kupczik, K., Dobson, C.A., Fagan, M.J., Crompton, R.H., Oxnard, C.E., O'Higgins, P., 2007. Assessing mechanical function of the zygomatic region in macaques: validation and sensitivity testing of finite element models. J. Anat. 210, 41–53 10.1111/j.1469-7580.2006.00662.x..

Kupczik, K., Dobson, C.A., Crompton, R.H., Phillips, R., Oxnard, C.E., Fagan, M.J., O'Higgins, P., 2009. Masticatory loading and bone adaptation in the supraorbital torus of developing macaques. Am. J. Phys. Anthropol. 139, 193–203.

Lansdown, D.A., Ding, Z., Wadington, M., Hornberger, J.L., Damon, B.M., 2007. Quantitative diffusion tensor MRI-based fiber tracking of human skeletal muscle. Eur. J. Appl. Physiol. 103, 673–681. http://dx.doi.org/10.1152/japplphysiol.00290.2007 (Bethesda, MD: 1985).

Lautenschlager, S., Bright, J.A., Rayfield, E.J., 2014. Digital dissection—using contrast-enhanced computed tomography scanning to elucidate hard- and soft-tissue anatomy in the Common Buzzard Buteo buteo. J. Anat. 224, 412–431. http://dx.doi.org/10.1111/Joa.12153.

Lee, D., Ravichandiran, K., Jackson, K., Fiume, E., Agur, A., 2012. Robust estimation of physiological cross-sectional area and geometric reconstruction for human skeletal muscle. J. Biomech. 45, 1507–1513.

Lexell, J., Downham, D.Y., 1991. The occurrence of fibre-type grouping in healthy human muscle: a quantitative study of cross-sections of whole vastus lateralis from men between 15 and 83 years. Acta Neuropathol. 81, 377–381. http://dx.doi.org/10.1007/BF00293457.

Lieber, R.L., Fridén, J., 2000. Functional and clinical significance of skeletal muscle architecture. Muscle Nerve 23, 1647–1666.

Manly, B.F.J., 2006. Randomization, Bootstrap and Monte Carlo Methods in Biology. CRC Press.

Metscher, B.D., 2009. MicroCT for developmental biology: a versatile tool for high-contrast 3D imaging at histological resolutions. Dev. Dyn. 238, 632–640. http://dx.doi.org/10.1002/Dvdy.21857.

Monti, R.J., Roy, R.R., Hodgson, J.A., Edgerton, V.R., 1999. Transmission of forces within mammalian skeletal muscles. J. Biomech. 32, 371–380.

Mordhorst, M., Heidlauf, T., Röhrle, O., 2015. Predicting electromyographic signals under realistic conditions using a multiscale chemo-electro-mechanical finite element model. Interface Focus 5, 20140076.

Namburete, A.I.L., Rana, M., Wakeling, J.M., 2011. Computational methods for quantifying in vivo muscle fascicle curvature from ultrasound images. J. Biomech. 44, 2538–2543. http://dx.doi.org/10.1016/j.jbiomech.2011.07.017.

Poelstra, K.A., Eijkelkamp, M.F., Veldhuizen, A.G., 2000. The geometry of the human paraspinal muscles with the aid of three-dimensional computed tomography scans and 3-Space Isotrak. Spine 25, 2176–2179.

Rana, M., Wakeling, J.M., 2011. In-vivo determination of 3D muscle architecture of human muscle using free hand ultrasound. J. Biomech. 44, 2129–2135. http://dx.doi.org/10.1016/j.jbiomech.2011.05.026.

Ravichandiran, K., Ravichandiran, M., Oliver, M.L., Singh, K.S., McKee, N.H., Agur, A. M.R., 2010. Fibre bundle element method of determining physiological cross-sectional area from three-dimensional computer muscle models created from digitised fibre bundle data. Comput. Methods Biomech. Biomed. Eng. 13, 741–748. http://dx.doi.org/10.1080/10255840903580025.

Röhrle, O., 2010. Simulating the electro-mechanical behavior of skeletal muscles. IEEE Comput. Sci. Eng. 12, 48–58.

Röhrle, O., Pullan, A.J., 2007. Three-dimensional finite element modelling of muscle forces during mastication. J. Biomech. 40, 3363–3372.

Ross, C.F., Patel, B.A., Slice, D.E., Strait, D.S., Dechow, P.C., Richmond, B.G., Spencer, M.A., 2005. Modeling masticatory muscle force in finite element analysis: sensitivity analysis using principal coordinates analysis. Anat. Rec. Part A: Discoveries Mol. Cell. Evol. Biol. 283, 288–299.

Sachse, F., Wolf, M., Werner, C., K.M.-W., 1998. Extension of anatomical models of the human body: three-dimensional interpolation of muscle fiber orientation based on restrictions. J. Comput. Inf. Technol. 6, 95–101.

Sánchez, C.A., Lloyd, J.E., Fels, S., Abolmaesumi, P., 2014. Embedding digitized fibre fields in finite element models of muscles. Comput. Methods Biomech. Biomed. Eng.: Imaging Visual., 1–14.

Schenk, P., Siebert, T., Hiepe, P., Güllmar, D., Reichenbach, J.R., Wick, C., Blickhan, R., Böl, M., 2013. Determination of three-dimensional muscle architectures: validation of the DTI-based fiber tractography method by manual digitization. J. Anat. 223, 61–68. http://dx.doi.org/10.1111/joa.12062.

Schumacher, G.-H., 1961. Funktionelle Morphologie der Kaumuskulatur. G. Fischer Verlag, Jena.

Sieben, J.M., van Otten, I., Lataster, A., Froeling, M., Nederveen, A.J., Strijkers, G.J., Drost, M.R., 2013. In vivo reconstruction of lumbar erector spinae architecture using diffusion tensor MRI. J. Spinal Disord. Tech. , http://dx.doi.org/10.1097/BSD.0000000000000036.

Siebert, T., Rode, C., Herzog, W., Till, O., Blickhan, R., 2008. Nonlinearities make a difference: comparison of two common Hill-type models with real muscle. Biol. Cybern. 98 133-14.

Stark, H., Schilling, N., 2010. A novel method of studying fascicle architecture in relaxed and contracted muscles. J. Biomech. 43, 2897–2903. http://dx.doi.org/10.1016/j.jbiomech.2010.07.031.

Stark, H., Fröber, R., Schilling, N., 2013. Intramuscular architecture of the autochthonous back muscles in humans. J. Anat. 222, 214–222. http://dx.doi.org/10.1111/joa.12005.

Strom, D., Holm, S., Clemensson, E., Haraldson, T., Carlsson, G.E., 1988. Gross-anatomy of the craniomandibular joint and masticatory muscles of the dog. Arch. Oral Biol. 33, 597–604 10.1016/0003-9969(88)90135-5.

R Core Team, 2014. R: A Language and Environment for Statistical Computing. Vienna, 2014.

Tsai, H.P., Holliday, C.M., 2011. Ontogeny of the alligator cartilago transiliens and its significance for sauropsid jaw muscle evolution. PLoS One 6, doi:ARTN e24935 DOI 10.1371/journal.pone.0024935.

Varela, M., Zhao, J., Aslanidi, O.V., 2013. Determination of atrial myofibre orientation using structure tensor analysis for biophysical modelling. Lect. Notes Comput. Sci. 7945, 425–432. http://dx.doi.org/10.1007/978-3-642-38899-6_50.

Vickerton, P., Jarvis, J., Jeffery, N., 2013. Concentration-dependent specimen shrinkage in iodine-enhanced microCT. J. Anat. 223, 185–193. http://dx.doi.org/10.1111/Joa.12068.

Ward, S.R., Lieber, R.L., 2005. Density and hydration of fresh and fixed human skeletal muscle. J. Biomech. 38, 2317–2320.